Threshold plasticity of SOI-GST microring resonators

ZILING FU,[1] **ZHI WANG,**[1,*] **PETER BIENSTMAN,**[2] **RUI JIANG,**[1] **TAO JIA,**[1] **HUIYING WANG,**[3] **CHAO SHANG,**[1] **AND CHONGQING WU**[1]

[1]*Institute of Optical Information, Key Laboratory of Luminescence and Optical Information, Ministry of Education, School of Physical Science and Engineering, Beijing Jiaotong University, Beijing 100044, China*
[2]*Photonics Research Group, Ghent University - IMEC, Ghent 9052, Belgium*
[3]*School of Optics and Photonics, Beijing Institute of Technology, Beijing 100081, China*
*zhiwang@bjtu.edu.cn

Abstract: Spiking Neural Networks, also known as third generation Artificial Neural Networks, have widely attracted more attention because of their advantages of behaving more biologically interpretable and being more suitable for hardware implementation. Apart from using traditional synaptic plasticity, neural networks can also be based on threshold plasticity, achieving similar functionality. This can be implemented using e.g. the Bienenstock, Cooper and Munro rule. This is a classical unsupervised learning mechanism in which the threshold is closely related to the output of the post-synaptic neuron. We show in simulations that the threshold characteristics of the nonlinear effects of a microring resonator integrated with $Ge_2Sb_2Te_5$ demonstrate some complex dependencies on the intracavity refractive index, attenuation, and wavelength detuning of the incident optical pulse, and exhibit class II excitability. We also show that we are able to modify the threshold power of the microring resonator by the changes of the refractive index and loss of $Ge_2Sb_2Te_5$, due to transitions between the crystalline and amorphous states. Simulations show that the presented device exhibits both excitatory and inhibitory learning behavior, either lowering or raising the threshold.

1. Introduction

Artificial neural networks (ANNs) have revolutionized the field of information technology, leading to the development of more optimized and autonomous artificial intelligence systems [1]. However, ANNs require a large amount of power to run on classic Von Neumann machines, even when using optimized hardware such as graphical processing units (GPUs) [2]. To address this issue, spiking neural networks (SNNs) were developed. They behave in a biologically more interpretable way and are more suitable for hardware implementation. These networks perform computations asynchronously, i.e. without an external clock. SNNs can run on neuromorphic processors, which allow for analog-like asynchronous communication. Several commercial solutions are now available, including Intel Loihi [3], IBM's TrueNorth [4], and SpiNNaker [5]. SNNs are orders of magnitude more energy-efficient than their non-spiking counterparts, which require constant energy consumption even when communication or computation is unnecessary.

At present, the learning mechanism of on-chip SNNs are mostly based on Spike-Timing-Dependent Plasticity (STDP) [6]. Various photonic synapses have demonstrated STDP behavior by changing the transmission levels of Phase Change Materials (PCMs) [7–10], which feature multiple stable phases of matter that have distinct optical properties. Changing the state of the PCM from amorphous to crystalline varies the waveguide's effective refractive index and modulates the absorption [11]. The most commonly used PCM is the archetypal alloy $Ge_2Sb_2Te_5$ [12–15].

Alternatively, SNNs can be based threshold plasticity rather than on synaptic plasticity. E.g., the Bienenstock, Cooper and Munro (BCM) rule is a classical unsupervised learning mechanism

that was developed based on the dynamic threshold phenomenon observed in biological vision systems [16]. Researchers have found that the threshold of neurons in these systems can change in response to environmental changes, allowing for better adaptation. In the BCM rule, the threshold is closely related to the output of the postsynaptic neuron [17]. G. Tesauro demonstrated that neural networks using threshold plasticity, rather than synaptic plasticity, can achieve the same functionality [18].

At present, a threshold plasticity learning mechanism based on BCM rules has been used in neural networks for phoneme recognition [19], 3D object recognition [20] and face recognition [21]. However, the neural networks of these reports are only based on simulations rather than physical implementations. In recent years, due to the unique device structure and memory characteristics of memristors, some feasible methods to implement sliding threshold have been proposed. $SrTiO_3$-based second-order memristors [22], memristive synapse model based on the HP memristor [23], WO_{3-x} memristive synapse [24] have been shown to achieve sliding threshold plasticity mechanism based on BCM rules. The realization of the threshold plasticity learning mechanism in the on-chip optical neural network is only based on our previous scheme using hybrid Si-VO_2 microring resonators [25]. However, due to the volatility of VO_2 [26,27], it does not offer any advantages in terms of power consumption.

In this paper, to address this issue, we use the non-volatility of the phase change material GST and its different refractive index and attenuation in different states [14,15,28] to realize an on-chip threshold plasticity learning mechanism. We numerically simulate the threshold plasticity of the nonlinear effects of a SOI microring integrated with GST. We design the all-pass microring resonator covered with GST and investigate the characteristics of its nonlinear phase plane and threshold plasticity, which can be tailored by the refractive index, attenuation and wavelength detuning of signal optical pulse. When we change the power of the optical signal pulse, the microring undergoes a subcritical Andronov-Hopf bifurcation. As a consequence, the system shows class II excitability. Therefore, the threshold power of the microring resonator is changed by the refractive index and loss of GST during the state change, and the device can be employed to implement excitatory and inhibitory learning mechanisms.

2. SOI-GST microring resonator

The excitable microring is mainly based on the combined effects of free carrier absorption (FCA), free carrier dispersion (FCD) and the thermo-optical (TO) effect. Moreover, the Coupled Mode Theory (CMT) model allows to incorporate the contributions of all the relevant physical effects in a very intuitive and accurate way [29]. Therefore, the CMT model is chosen to simulate these physical effects in the excitable microring. An all-pass microring resonator loaded with the phase change material GST was designed on the SOI platform as shown in Fig. 1. The resonator had a radius of 50 μm, the silicon waveguide height is of 220 nm, and the gap between the microring and the bus waveguide is of 600 nm. GST was deposited on the microring with a thickness of 10 nm and a length of 100 nm, and an ITO cap with a thickness of 10 nm was deposited to avoid oxidation.

In a previous study [30], the Coupled Mode Theory (CMT) model was used to analyze the propagation of transverse electric (TE) mode incident pulses in an add-drop microring resonator loaded with GST. However, for an all-pass microring loaded with GST, which consists of a single ring coupled with only one bus waveguide, the CMT equation is simplified as follows:

$$
\begin{aligned}
\frac{\partial u}{\partial t} &= \left[i\delta\omega_{nl\_hy} + i(\omega_{r\_hy} - \omega) - \frac{\gamma_{loss\_hy}}{2} \right] u + \kappa S_{in}, \\
\frac{\partial N}{\partial t} &= -\frac{N}{\tau_{fc}} + \frac{\beta_{Si}c^2}{2\,\hbar\omega V_{FCA}^2 n_{g\_hy}^2} |u|^4, \\
\frac{\partial \Delta T}{\partial t} &= -\frac{\Delta T}{\tau_{th}} + \frac{\gamma_{abs\_hy}|u|^2}{\rho_{Si}c_{p,Si}V_{th}},
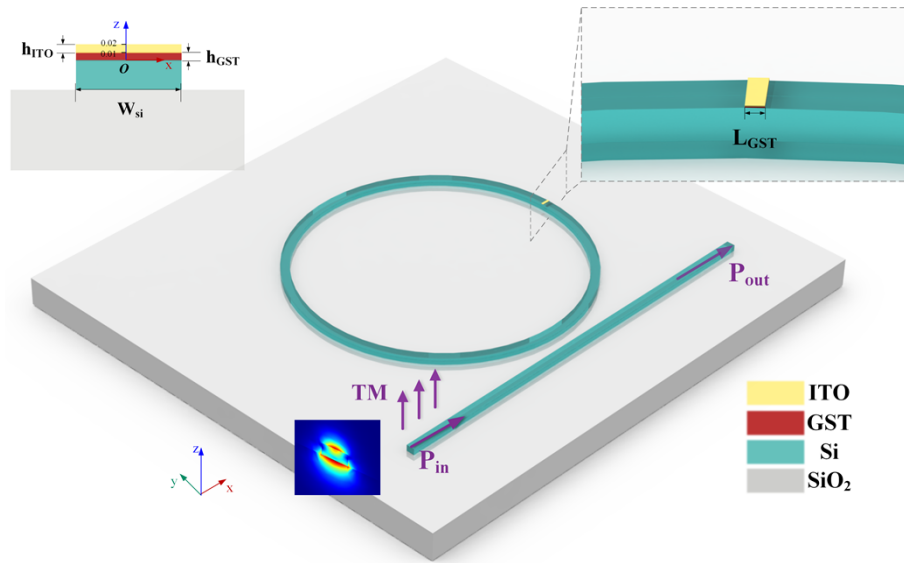\end{aligned}
\tag{1}
$$

Fig. 1. SOI-GST Microring resonator. Inset: cross-section and zoom-in of the GST cell.

where u is the temporal evolution of the intracavity field, N is the free-carrier density, and ΔT is the temperature change in the GST-loaded microring resonator.

Compared to a GST-loaded add-drop microring resonator, the main difference in an all-pass microring resonator is that there is less coupling loss due to the presence of only one bus waveguide. Therefore, the total loss γ_{loss_hy} of the GST-loaded all-pass microring is:

$$\gamma_{loss\_hy} = \gamma_{coup} + \gamma_{rad} + \gamma_{abs\_hy}$$
$$\gamma_{abs\_hy} = \gamma_{abs,lin} + \gamma_{abs,FCA} + \gamma_{abs,TPA}$$

(2)

Other parameters and expressions in Eq. (1) are consistent with those given in Ref. [30].

A finite-difference time-domain (FDTD) simulation was employed to calculate the electric field distribution E in the GST [12]. The evanescent-field coupling and power (heat) transfer between the guided light and the GST were investigated by calculating the unit power absorption (P_{abs}) [31,32].

Figure 2 shows the calculated P_{abs} in amorphous and crystalline GST for a 1 mW input power using transverse magnetic (TM) and transverse electric (TE) modes as input, as the width of the GST-cell varies from 440 nm to 640 nm. The waveguide supports one TE-like and one TM-like mode in this range at a wavelength of 1550 nm. P_{abs} is obtained by integrating the power loss density over the area of the GST-cell. As crystalline GST has a larger complex refractive index in the C band, and the overlapping area between the GST-cell and light field is larger with a TM mode input optical pulse, it is observed that for the same state of GST, the power absorption of the TM mode is larger than that of the TE mode. For each particular mode, the power absorption of crystalline GST is larger than that of amorphous. The maximum optical power absorbed by the GST-cell occurs when the waveguide width is about 600 nm, as shown in Fig. 2. A waveguide width of 600 nm was chosen to obtain larger power absorption. For the rest of the paper, the TM mode was chosen over the TE mode due to its larger P_{abs} in the GST and larger amplitude coupling coefficients in the microring resonator, resulting in a lower threshold and power consumption.
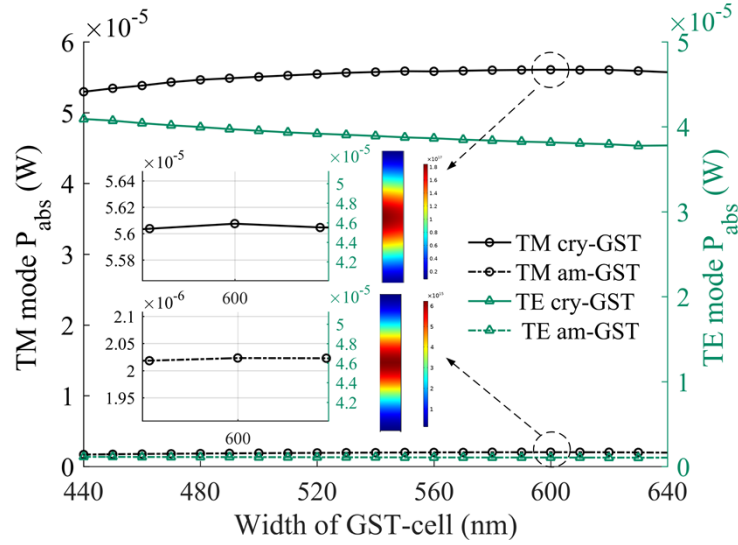
Fig. 2. Calculated results of the unit power absorption P_{abs} for the TM (black circle) and TE (green triangle) mode, for an amorphous (dotted line) and crystalline (solid line) GST-cell, as the waveguide width varies from 440 nm to 640 nm. Inset: zoomed-in region of the black circle, showing the unit power absorption P_{abs} at the center of the amorphous and crystalline GST using the TM mode input optical pulse.

3. Nonlinear phase-plane and threshold characteristics

A SOI microring resonator can show Class II excitability [29,33], for which the shape of the input perturbation (stimulus) does not need to be precisely controlled. Indeed, as long as the input perturbation is sufficiently strong, the shape of the ring's excitation is hardly affected by the shape of the input pulse. Therefore, only a Continuous Wave (CW) input was considered in the bifurcation analysis for Class II excitability.

Setting the derivatives to zero in Eq. (1) results in the steady state equations:

$$
\begin{aligned}
\left[(\delta\omega_{nl\_hy} + \omega_{r\_hy} - \omega)^2 - \left(\frac{\gamma_{loss\_hy}}{2} \right)^2 \right] u - |\kappa S_{in}|^2 &= 0, \\
-\frac{N}{\tau_{fc}} + \frac{\beta_{Si} c^2}{2\, \hbar\omega V_{FCA}^2 n_{g\_hy}^2} |u|^4 &= 0, \\
-\frac{\Delta T}{\tau_{th}} + \frac{\gamma_{abs\_hy} |u|^2}{\rho_{Si} c_{p,Si} V_{th}} &= 0.
\end{aligned}
\tag{3}
$$

The Fixed Points (FP) u, ΔT and N of the system can be solved using Eq. (3). The stability of the steady state solutions can be analyzed by evaluating the eigenvalues of the Jacobian of the system equations. Between u, ΔT and N of the system, the rate of change of u is much faster than that of ΔT and N. Therefore, the system state rapidly jumps to the zero-growth curve of $du/dt = 0$ with the input perturbation. For this purpose, we project the $(u, \Delta T, N)$ -time-traces for a given input power and wavelength onto the $(\Delta T, N)$-plane. Thus, the projection of zero-growth curves of $d(N, u)/dt = 0$ and $d(\Delta T, u)/dt = 0$ on the $(\Delta T, N)$ phase-plane can be considered to analyze the dynamic characteristics of the system. When solving $d(N, u)/dt = 0$, the second equation of Eq. (1) was used to parameterize N as a function of u. This was substituted into the first equation of Eq. (3) and solved for ΔT as a quadratic equation. By scanning the value of ΔT, the projection of $d(N, u)/dt = 0$ on the $(\Delta T, N)$ phase-plane can be obtained. For the solution of $d(\Delta T, u)/dt = 0$, a parameterization of ΔT and N as a function of u was used [25,29].

The $d(N, u)/dt = 0$ and $d(\Delta T, u)/dt = 0$ nullclines were calculated for a wavelength shift of -20 pm in the am-GST-loaded microring. Here, the Runge-Kutta method is used directly to calculate Eq. (1). The optical input power is 0.8 mW for Fig. 3 and 1.5 mW for Fig. 4. The optical energy $|u|^2$, the concentration of free carriers N and the mode-averaged temperature difference with the surroundings ΔT change with time were shown in Fig. 3(b) and Fig. 4(b). The impulse response is measured by the maximum temperature change ΔT_{max} caused by P_{in}. The threshold is defined as the optical pulse power P_{th} at which $d\Delta T_{max}/dP_{in}$ reaches its maximum value, i.e., when the change in ΔT_{max} is at its maximum.
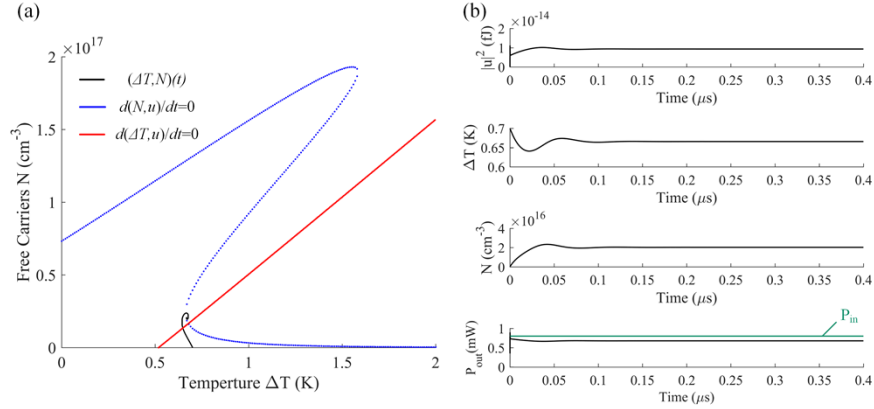

Fig. 3. (a) (ΔT, N) plane and (b) dynamic response of microring resonator when $\Delta\lambda$=-20 pm and $P_{in} = 0.8$ mW (below threshold).
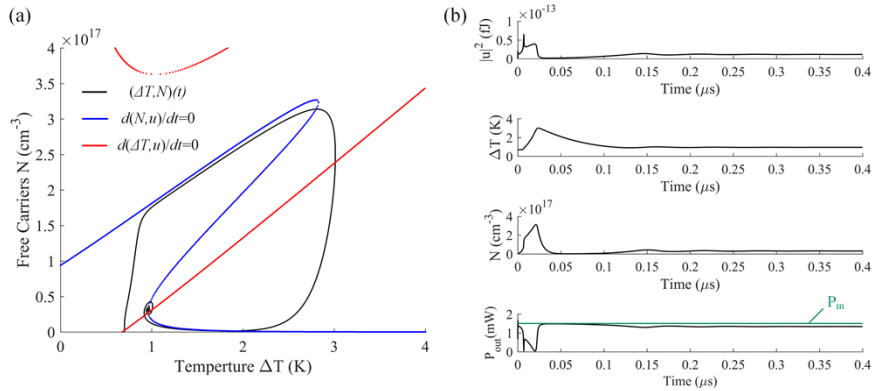

Fig. 4. (a) (ΔT, N) plane and (b) dynamic response of microring resonator when $\Delta\lambda$=-20 pm and $P_{in} = 1.5$ mW (above threshold).

The threshold characteristics of a microring loaded with GST are obvious from Figs. 3 (below threshold) and 4 (above threshold). Indeed, it is shown in Fig. 3 that the system only has one stable fixed point (FP), and the optical pulse power does not reach the threshold. There is no impulse response output in the microring, and ΔT and N are almost unchanged. The microring capped with am-GST is in the sub-threshold state.

On the other hand, in Fig. 4 the microring produces an impulse output response, and the maximum value of ΔT exhibits a jump. This is primarily due to the fact that the rate of change of N is much faster than that of ΔT. The time traces often relax towards the $d(N, u)/dt = 0$ nullcline

and eventually return to a stable FP through oscillation. As a result of the microring undergoing a Saddle-Node bifurcation (SN), the stable and unstable Limit Cycle (LC) annihilate in a fold LC bifurcation. However, due to its proximity to the fold LC bifurcation, the system can exhibit excitability under external stimulation in this regime.

When the incident light pulse power is further increased to $P_{in} = 2.3$ mW, a stable LC coexists with a stable FP centered in this LC, as shown in Fig. 5. This indicates a subcritical Andronov-Hopf bifurcation. We prove explicitly with time-traces that the LC encloses a stable FP in the $(\Delta T, N)$ phase-plane. Depending on the initial conditions, the time-trace will converge to the stable LC (black curve $(\Delta T, N)$ $(t = 0) = (1.1$ K, $4e^{16}$ cm^{-3})) or to the stable FP (magenta curve $(\Delta T, N)$ $(t = 0) = (1.4$ K, $4e^{16}$ cm^{-3})). The pulse trajectories in the phase plane in Fig. 5(b) also clearly illustrate it. Therefore, when P_{in} is set close to a subcritical Andronov-Hopf bifurcation, similar to the excitability reported in Ref. [34], the microring system can exhibit Class II excitability [35].
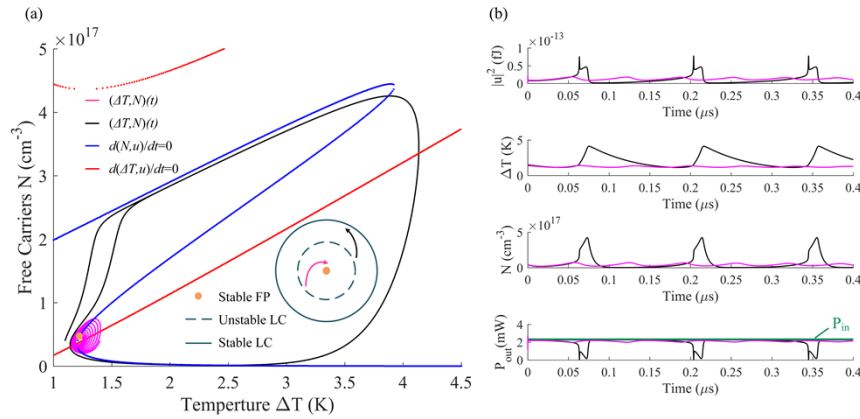

Fig. 5. (a) $(\Delta T, N)$ plane and (b) dynamic response of microring resonator at $P_{in} = 2.3$ mW, the initial conditions of black curve and magenta curve correspond to $(\Delta T, N)$ $(t = 0) = (1.1$ K, $4e^{16}$ cm−3) and $(\Delta T, N)$ $(t = 0) = (1.4$ K, $4e^{16}$ cm^{-3}) respectively.

With the increase of the input optical power perturbation, self-pulsation occurs. In Fig. 6, we calculate the $(\Delta T, N)$ plane and dynamic response when the input optical power perturbation P_{in} is 3 mW. At this point, the microring resonator is in the self-pulsation regime. The system has a stable limit cycle, and it exhibits self-pulsation behavior in this interval.

Finally, Fig. 7 (a) shows the dependence of the threshold of microring resonators coated with GST on the crystallization fraction. The results demonstrate that, when the detuning of the incident light pulse remains constant, the threshold of the microring increases as the GST crystallization fraction increases, which can be attributed to the higher loss of higher crystalline fraction.

However, according to the third expression of Eq. (1), an increase in cavity loss results in an increase in temperature change, which in turn leads to a decrease in the negative value of $\delta\omega_{nl\_hy}$. According to Eq. (4), this can be considered equivalent to a blue shift in the signal optical wavelength.

$$\delta\omega_{nl\_hy} = -\frac{\omega}{n_{g\_mix}} \left(\frac{dn_{si}}{dT} \Delta T + \frac{dn_{si}}{dN} N \right). \tag{4}$$

The threshold of microring covered with GST is related to the wavelength λ as well, as also shown in Fig. 7(a). In principle, the threshold power P_{th} increases as $\Delta\lambda$ (λ detuned from resonant wavelength λ_r) increases.
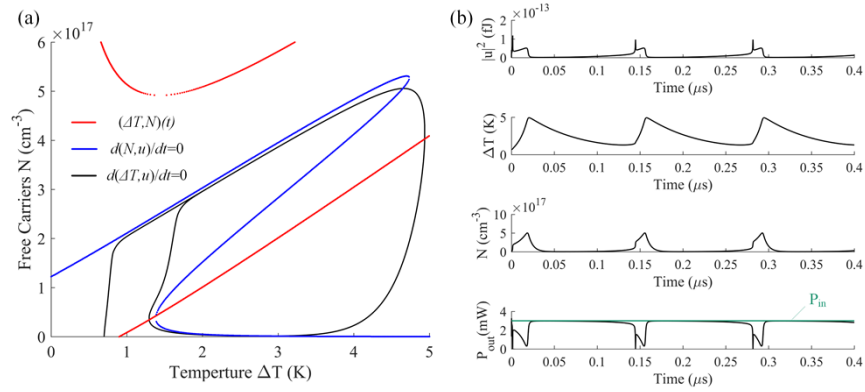
Fig. 6. (a) (ΔT, N) plane and (b) dynamic response of microring resonator when $\Delta\lambda$=-20 pm and $P_{in} = 3$ mW (above threshold).
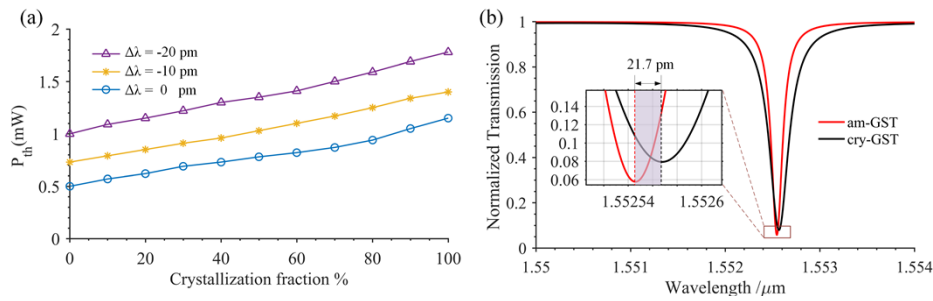

Fig. 7. (a)Threshold of optical spiking ring changes with the crystallized fraction of am-GST-loaded microring. (b) The resonance wavelength shifts between the microring integrated with am-GST and cry-GST. The inset clearly shows an enlarged view of the transmission characteristics to show the wavelength shift.

Given the microring resonator parameters, if the input optical pulse is detuned towards the blue, typically a subcritical Andronov-Hopf bifurcation that can achieve Class II excitability appears. However, if the input optical pulse is detuned towards the red, a supercritical Andronov-Hopf bifurcation appears [33,36]. Therefore, for the realization of the threshold plasticity learning mechanism, it is required to always maintain $\Delta\lambda$<0. Note that there is a wavelength shift of 21.7 pm between the resonance wavelength of microring integrated with am-GST and cry-GST, as shown in Fig. 7 (b). Therefore, we choose $\Delta\lambda$ = -20pm, so that the system has $\Delta\lambda < 0$ in any state of GST to achieve subcritical Andronov-Hopf bifurcation.

4. Learning behavior

As we have seen in the previous section, when the power of the optical signal pulse reaches the threshold of the microring, the resulting temperature change is considerably greater than when the microring does not respond, causing a significant change in the loss of the Si-GST waveguide. As we will show now, this effect can be used to increase or decrease the threshold of the microring, depending on the initial crystallization state. This process can be applied to a threshold plasticity learning mechanism.

4.1. Inhibitory learning behavior

To show inhibitory learning (increased threshold), we start from a microring with GST in the amorphous phase. We inject a series of square light pulses with varying power levels, detuned by $\Delta\lambda$=-20 pm, and having a pulse width of 100 ns. Figure 8 (a) top shows the injected pulses, and (a) bottom shows the output of the microring. At first, an injected pulse with a power of 1.1 mW can elicit a response from the microring, as can be seen by the short drop in output. However, after injecting a high-power signal optical pulse of 50 mW, partial crystallization of GST results in an increase in intracavity loss and consequently an increase in threshold. Concurrently, partial crystallization of GST causes a decrease in the red shift $\Delta\lambda$ (negative value) of the resonant wavelength of the microring resonator cavity, resulting in an increased threshold. At this point, an injected optical pulse with a power of 1.1 mW is no longer capable of eliciting a response from the microring. Injecting a signal optical pulse with higher power can further increase the threshold of this microring.
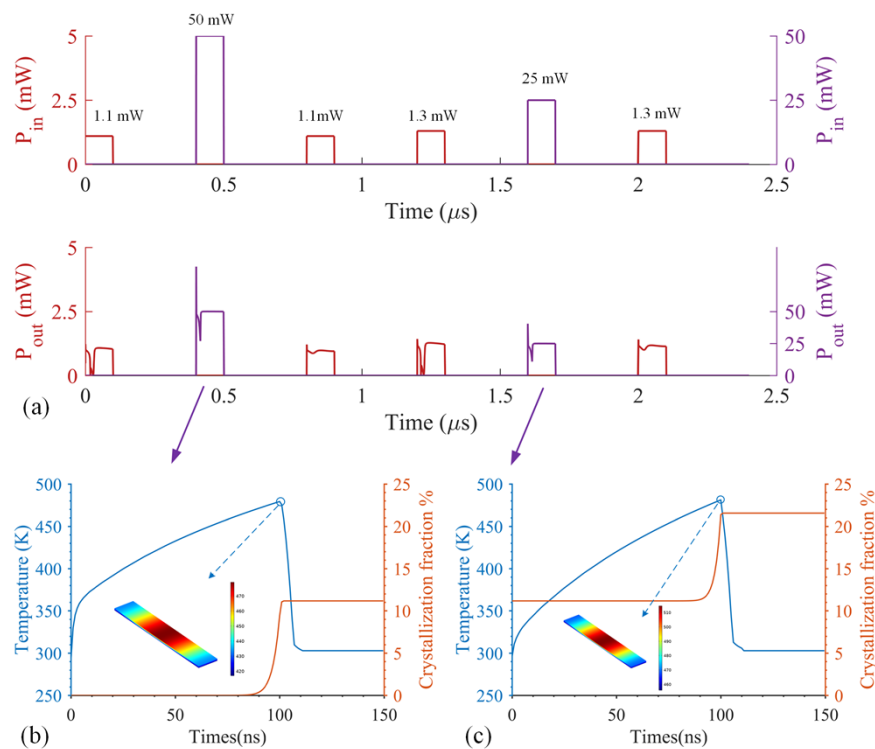

Fig. 8. (a) Injection perturbation signal and the response of spiking ring induced by injection perturbation; The crystallization fraction and temperature change of the GST cell when the optical pulse is (b) 50 mW and (c) 25 mW.

To simulate the process of high-power optical pulses inducing phase transitions of am-GST, we use the Johnson-Mehl-Avrami Kohnogorov (JMAK) model [37]. Figure 8(b) shows the simulated changes in the average temperature and crystallization fraction of the GST deposited on the microring caused by a 50 mW optical pulse. The temperature distribution of the GST at the end of the signal pulse is shown in the inset of Fig. 8(b), which illustrates that the maximum temperature difference of GST is less than 10% at this time. Hence, we use the average temperature of GST to calculate its crystallization fraction, and thus obtain the changes in the refractive index and loss of the Si-GST hybrid waveguide. Figure 8(c) shows the changes in the average temperature

and crystallization fraction of GST induced by a following optical pulse of 25 mW for further crystallization over time.

4.2. Excitatory learning behavior

On the other hand, to show excitatory behavior, we start from GST in the crystalline state instead. The width of pulses is also 100 ns. Figure 9(a) top shows the optical injected signal, and (a) bottom shows the output of the microring. Initially, an injected light pulse with a power of 1.7 mW cannot make the microring produce a response. However, after an 8 mW optical pulse is injected, the loss in the cavity increases and the threshold decreases due to the partial amorphization of GST. At the same time, the blue shift $\Delta\lambda$ (negative value) of the resonant wavelength of the microring is increased due to the partial amorphous GST, which also leads to a decrease of the threshold. At this time, an incident optical pulse with the same power as before (1.7 mW) can make the microring produce an output. At this point in time, the threshold of the microring resonator is higher than 1.6 mW, as injecting such a pulse does not elicit any response. However, the threshold of the microring can be further reduced by injecting a 9 mW optical pulse, so that 1.6 mW injection signal pulse can new also make the microring produce a response.
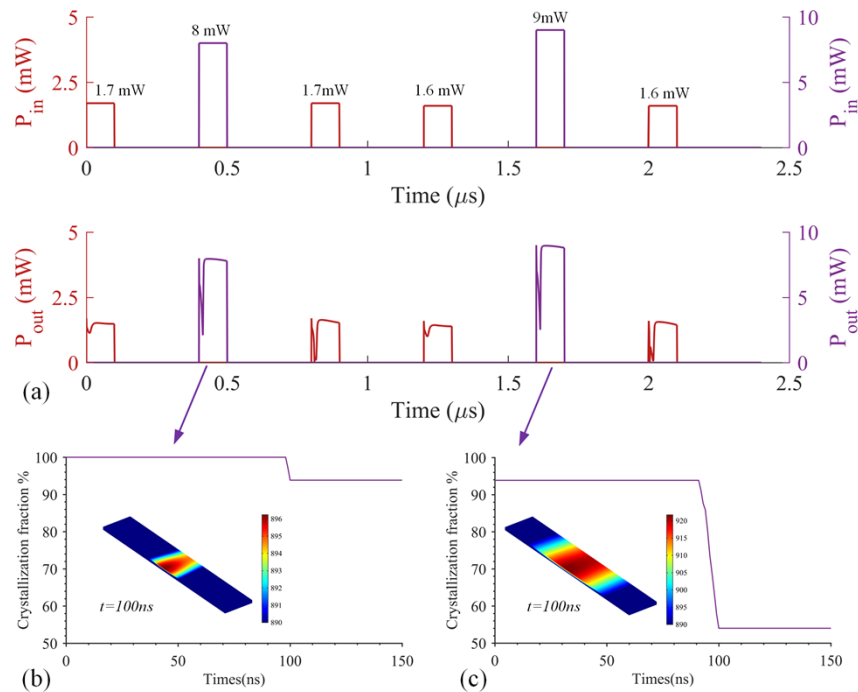

Fig. 9. (a) Injection perturbation signal and the response of spiking ring induced by injection perturbation; The crystal fraction of the GST cell when the optical pulse is (b) 8 mW and (c) 9 mW.

In the process of GST transitioning from a crystalline to an amorphous state, high-power light pulses first heat GST to above the melting temperature (~890 K) [31], causing the chemical bonds in the crystalline GST material to break, and then undergo a rapid cooling quenching process, so that the atoms in the molten state do not have time to rearrange into bonds, thus forming a short-range ordered but long-range disordered amorphous state. Therefore, we use the volume ratio of the region that is heated above the melting temperature and quickly cooled to amorphize as the percentage of amorphization, as shown in the inset of Fig. 9(b), to obtain the change in

GST's crystallization fraction over time, and thus obtain the changes in the refractive index and loss of the Si-GST hybrid waveguide.

5.   Conclusion

We conducted numerical simulations to investigate the threshold plasticity of nonlinear all-pass microrings integrated with GST. We discussed its phase plane and threshold characteristics. The results demonstrated that the threshold characteristics of the microring resonator depend on the refractive index, attenuation, and wavelength detuning of the input signal. When the power of the optical pulse is adjusted precisely, the microring shows subcritical Andronov-Hopf bifurcation dynamics, resulting in class II excitability. Consequently, the threshold power of the microring resonator can be modified by changing the refractive index and loss of GST during state transitions. The threshold plasticities of this kind of microring exhibit both excitatory and inhibitory learning behavior, providing a feasible path towards emulating BCM learning rules in photonic SNNs.

Disclosures. The authors declare no conflicts of interest.

Data availability. Data underlying the results presented in this paper are not publicly available at this time but may be obtained from the authors upon reasonable request

Reference

1. O. I. Abiodun, A. Jantan, and A. E. Omolara, *et al.*, "State-of-the-art in artificial neural network applications: A survey," Heliyon **4**(11), e00938 (2018).
2. A. Mehonic, A. Sebastian, and B. Rajendran, *et al.*, "Memristors—From In-Memory Computing, Deep Learning Acceleration, and Spiking Neural Networks to the Future of Neuromorphic and Bio-Inspired Computing," Advanced Intelligent Systems **2**(11), 2000085 (2020).
3. M. Davies, N. Srinivasa, and T.-H. Lin, *et al.*, "Loihi: A Neuromorphic Manycore Processor with On-Chip Learning," IEEE Micro **38**(1), 82–99 (2018).
4. P. A. Merolla, J. V. Arthur, and R. Alvarez-Icaza, *et al.*, "A million spiking-neuron integrated circuit with a scalable communication network and interface," Science **345**(6197), 668–673 (2014).
5. E. Painkras, L. A. Plana, and J. Garside, *et al.*, "SpiNNaker: A multi-core System-on-Chip for massively-parallel neural net simulation," *Proceedings of the IEEE 2012 Custom Integrated Circuits Conference* 1–4 (2012).
6. R. Toole, A. N. Tait, and T. Ferreira de Lima, *et al.*, "Photonic Implementation of Spike-Timing-Dependent Plasticity and Learning Algorithms of Biological Neural Systems," J. Lightwave Technol. **34**(2), 470–476 (2016).
7. I. Chakraborty, G. Saha, and K. Roy, "Photonic In-Memory Computing Primitive for Spiking Neural Networks Using Phase-Change Materials," Phys. Rev. Appl. **11**(1), 014063 (2019).
8. I. Chakraborty, G. Saha, and A. Sengupta, *et al.*, "Toward Fast Neural Computing using All-Photonic Phase Change Spiking Neurons," Sci. Rep. **8**(1), 12980 (2018).
9. J. Feldmann, N. Youngblood, and C. D. Wright, *et al.*, "All-optical spiking neurosynaptic networks with self-learning capabilities," Nature **569**(7755), 208–214 (2019).
10. Z. Cheng, C. Ríos, and W. H. P. Pernice, *et al.*, "On-chip photonic synapse," Sci. Adv. **3**(9), e1700160 (2017).
11. S. Raoux and M. Wuttig, *Phase Change Materials Science and Applications* (Springer, 2009, Chapter 9).
12. C. Rios, P. Hosseini, and C. D. Wright, *et al.*, "On-Chip Photonic Memory Elements Employing Phase-Change Materials," Adv. Mater. **26**(9), 1372–1377 (2014).
13. C. D. Wright, P. Hosseini, and J. A. V. Diosdado, "Beyond von-Neumann Computing with Nanoscale Phase-Change Memory Devices," Adv. Funct. Mater. **23**(18), 2248–2254 (2013).
14. N. Youngblood, C. Ríos, and E. Gemo, *et al.*, "Tunable Volatility of $Ge_2Sb_2Te_5$ in Integrated Photonics," Adv. Funct. Mater. **29**(11), 1807571 (2019).
15. W. H. P. Pernice and H. Bhaskaran, "Photonic non-volatile memories using phase change materials," Appl. Phys. Lett. **101**(17), 171101 (2012).
16. E. L. Bienenstock, L. N. Cooper, and P. W. Munro, "Theory for the development of neuron selectivity: orientation specificity and binocular interaction in visual cortex," J. Neurosci. **2**(1), 32–48 (1982).
17. L. N. Cooper and M. F. Bear, "The BCM theory of synapse modification at 30: interaction of theory with experiment," Nat. Rev. Neurosci. **13**(11), 798–810 (2012).
18. G. Tesauro, "A plausible neural circuit for classical conditioning without synaptic plasticity," Proc. Natl. Acad. Sci. U. S. A. **85**(8), 2830–2833 (1988).
19. F. Alibart, E. Zamanidoost, and D. B. Strukov, "Pattern classification by memristive crossbar circuits using ex situ and in situ training," Nat. Commun. **4**(1), 2072 (2013).

20. M. Prezioso, F. Merrikh-Bayat, and B. D. Hoskins, *et al.*, "Training and operation of an integrated neuromorphic network based on metal-oxide memristors," Nature **521**(7550), 61–64 (2015).
21. M. Hu, C. E. Graves, and C. Li, *et al.*, "Memristor-Based Analog Computation and Neural Network Classification with a Dot Product Engine," Adv. Mater. **30**(9), 1705914 (2018).
22. J. Xiong, R. Yang, and J. Shaibo, *et al.*, "Bienenstock, Cooper, and Munro Learning Rules Realized in Second-Order Memristors with Tunable Forgetting Rate," Adv. Funct. Mater. **29**(9), 1807316 (2019).
23. Y. Huang, J. Liu, and J. Harkin, *et al.*, "An memristor-based synapse implementation using BCM learning rule," Neurocomputing **423**, 336–342 (2021).
24. Z. Wang, T. Zeng, and Y. Ren, *et al.*, "Toward a generalized Bienenstock-Cooper-Munro rule for spatiotemporal learning via triplet-STDP in memristive devices," Nat. Commun. **11**(1), 1510 (2020).
25. Z. Wang, Q. Li, and Z. Fu, *et al.*, "Threshold plasticity of hybrid Si-VO2 microring resonators," in *Optical Fiber Communication Conference (OFC) 2020* (OSA, 2020), p. Th2A.26.
26. J. D. Ryckman, V. Diez-Blanco, and J. Nag, *et al.*, "Photothermal optical modulation of ultra-compact hybrid Si-VO$_2$ ring resonators," Opt. Express **20**(12), 13215–13225 (2012).
27. T. Driscoll, H.-T. Kim, and B.-G. Chae, *et al.*, "Memory Metamaterials," Science **325**(5947), 1518–1521 (2009).
28. C. Ríos, M. Stegmaier, and P. Hosseini, *et al.*, "Integrated all-photonic non-volatile multi-level memory," Nat. Photonics **9**(11), 725–732 (2015).
29. T. V. Vaerenbergh, M. Fiers, and P. Mechet, *et al.*, "Cascadable excitability in microrings," Opt. Express **20**(18), 20292 (2012).
30. Z. Fu, Z. Wang, and P. Bienstman, *et al.*, "Programmable low-power consumption all-optical nonlinear activation functions using a micro-ring resonator with phase-change materials," Opt. Express **30**(25), 44943 (2022).
31. C. Rios, M. Stegmaier, and Z. Cheng, *et al.*, "Controlled switching of phase-change materials by evanescent-field coupling in integrated photonics," Opt. Mater. Express **8**(9), 2455–2470 (2018).
32. Z. Cheng, C. Ríos, and N. Youngblood, *et al.*, "Device-Level Photonic Memories and Logic Applications Using Phase-Change Materials," Adv. Mater. **30**(32), 1802435 (2018).
33. T. Van Vaerenbergh, *All-optical spiking neurons integrated on a photonic chip*, (Ghent University, 2014).
34. M. Brunstein, A. M. Yacomotti, and I. Sagnes, *et al.*, "Excitability and self-pulsing in a photonic crystal nanocavity," Phys. Rev. A **85**(3), 031803 (2012).
35. E. M. Izhikevich, *Dynamical Systems in Neuroscience: The Geometry of Excitability and Bursting* (The MIT Press, 2006).
36. T. J. Johnson, M. Borselli, and O. Painter, "Self-induced optical modulation of the transmission through a high-Q silicon microdisk resonator," Opt. Express **14**(2), 817–831 (2006).
37. S. G.-C. Carrillo, E. Gemo, and X. Li, *et al.*, "Behavioral modeling of integrated phase-change photonic devices for neuromorphic computing applications," APL Mater. **7**(9), 091113 (2019).